THE ASTROPHYSICAL JOURNAL, 399:231–245, 1992 November 1

THE BOW SHOCK AND MACH DISK OF HH 34

JON A. MORSE[1]
Department of Physics and Astronomy, University of North Carolina, CB 3255, Phillips Hall, Chapel Hill, NC 27599-3255
PATRICK HARTIGAN
Department of Astronomy, University of Massachusetts, Amherst, MA 01003
GERALD CECIL[1]
Department of Physics and Astronomy, University of North Carolina, CB 3255, Phillips Hall, Chapel Hill, NC 27599-3255
JOHN C. RAYMOND
Harvard-Smithsonian Center for Astrophysics, 60 Garden Street, Cambridge, MA 02138
AND
STEVE HEATHCOTE
Cerro Tololo Inter-American Observatory, Casilla 603, La Serena, Chile
Received 1992 February 18; accepted 1992 May 8

ABSTRACT

We have used the Rutgers/CTIO imaging Fabry-Perot interferometer to acquire spatially resolved line profiles across the bow shock and Mach disk of the Herbig-Haro object HH 34 in [O III] λ5007, Hα, and [S II] $\lambda\lambda$6716, 6731. Profiles were obtained with $\sim$1.″5 spatial and 35 km s^{-1} FWHM velocity resolution. We have separated the Mach disk emission in this outflow from the bow shock emission both spatially and kinematically. Our observations provide the first detailed kinematic information about the shocked material behind the Mach disk of a stellar jet. The preshock gas to the south of HH 34 must flow outward at $\sim$150 km s^{-1} with respect to the stellar energy source to account for the observed kinematics of the line emission in HH 34. Hence, HH 34 is probably a secondary ejection that moves into the outflowing wake of an earlier ejection, a scenario also proposed by Heathcote & Reipurth to explain proper motions in HH 34. Our new measurements of the electron density as a function of position and velocity, combined with new models of the bow shock emission, show that the magnetic field inhibits the compression of the post–bow shock gas. We estimate the ambient magnetic field to be 10–20 μG in front of HH 34. The magnetic energy density in the preshock gas is less than 10^{-3} of the ram pressure, which implies that the magnetic field is not important in the flow dynamics of HH 34. By balancing the ram pressures in the bow shock and Mach disk, we estimate the jet-to-ambient density ratio $\eta \sim 10$. This is $\sim$10 times higher than previous estimates for η in this outflow.

Subject headings: ISM: kinematics and dynamics — stars: ISM: magnetic fields — shock waves — stars individual (HH 34) — stars: pre–main-sequence

1. INTRODUCTION

Astrophysical jets jets span an enormous range of scales and energetics, from relativistic extragalactic jets to collimated outflows emanating from newly formed stars. Despite this extensity in scale, a single theoretical framework may describe how these flows evolve and interact with their intergalactic or interstellar environments. The collimated outflows from nascent stars are ideal for studying jet dynamics because their densities are high enough ($\sim 10^3$–10^4 cm^{-3}) and velocities low enough (hundreds of km s^{-1}) for the shocks to radiate efficiently at optical wavelengths. Thus, the velocity and density structure of these jets can be traced by observing the emission lines of the postshock gas. The emitting regions are often several arcseconds in extent, so can be studied in detail using ground-based observations.

The region where the jet terminates and collides with the ambient medium is called the "working surface" (Blandford & Rees 1974). For a more or less continuous flow, two strong shock systems should form in the working surface: a bow shock that accelerates and excites ambient gas, and an inner shock or Mach disk that decelerates the jet material. Many bow-shaped Herbig-Haro (HH) objects are associated with the heads of radiative stellar jets (e.g., HH 1, HH 34, HH 47; see Mundt, Brugel, & Bührke 1987, and references therein). Additional knots of emission are often aligned in a "jet" that emanates from the vicinity of the stellar energy source powering the entire emission complex (e.g., HH 34, HH 111; see Reipurth 1989a). This energy source may be optically obscured but is usually detectable at infrared wavelengths.

Herbig-Haro objects provide an opportunity to study the working surfaces in highly supersonic, compressible, radiating flows. Observational constraints on jet physics are important because a full theoretical treatment involves solving the three-dimensional time-dependent hydrodynamical flow problem with proper consideration of ionization, magnetic fields, and radiative transfer. Two-dimensional hydrodynamical simulations indicate that a multitude of shocks form within the jet and at the working surface. In these calculations magnetic fields have either been ignored (e.g., Blondin, Fryxell, & Königl 1990) or assumed to completely dominate the dynamics (e.g., Lind et al. 1989). The numerical simulations predict a complex

[1] Visiting Astronomer, Cerro Tololo Inter-American Observatory, operated by the National Optical Astronomy Observatories under contract to the National Science Foundation.

and time-dependent flow in the Mach disk. However, existing observations of jets do not constrain the simulations, either because the Mach disk and bow shock do not radiate in emission lines (as in extragalactic jets), or the spatial and velocity resolution are not adequate to unambiguously separate the Mach disk and bow shocks (as in previous studies of stellar jets).

In this paper we report new observations of the HH 34 working surface, the most prominent region among the multiple working surfaces recently discovered in the HH 34 system. With Fabry-Perot area spectrophotometry, we are able to spatially resolve the velocity field, emission-line fluxes and line ratios at every point in the *volume* delineated by the working surface. In § 2, we discuss our observing techniques and data reductions and summarize previous investigations of the HH 34 system. In § 3, we present our new spectral grids and spatially complete maps of the electron density and [S II]/Hα ratio. In § 4, we discuss our model of the bow shock, constructed from new planar shock models that are optimized for this system. We assess the dynamical importance of the ambient magnetic field by comparing our data in detail with this bow shock model. We also present strong evidence for separate Mach disk and bow shock emission in HH 34. Section 5 summarizes our results. Our observations and analysis of the HH 34 jet will appear in a subsequent manuscript.

2. OBSERVATIONS AND REDUCTIONS

2.1. *Previous Observations of the HH 34 Complex*

The HH 34 complex is one of the best examples of an optical outflow from a young stellar object (YSO). It was first studied in detail by Reipurth et al. (1986), who drew attention to a luminous, highly collimated jet associated with the bow-shaped nebula labeled HH 34 (Herbig 1974). The visible knotty jet extends $\sim 26''$ from an optically faint YSO and points toward the bright *blueshifted* bow shock HH 34 (see Fig. 1) at a distance of $\sim 110''$. They identified several bright condensations in the visible jet and HH 34 and found low-excitation emission in the spectra of both regions that is typical of shock excitation. They also identified the energy source as a low-mass, emission-line, pre–main sequence star with a bolometric luminosity of $\sim 0.5\ L_{\odot}$. They could not associate a CO outflow, H_2 emission or radio continuum with HH 34. Optical polarization studies by Scarrott (1988) of the HH 34 nebula confirm that it is not a reflection nebula, unlike much of the faint emission near the energy source.

Deep CCD images by Bührke, Mundt & Ray (1988, hereafter BMR) have subsequently revealed a similar, though much fainter, *redshifted* bow shock HH 34N. It lies at nearly the same projected distance as HH 34 on the opposite side of the source. The lack of an observed redshifted jet and the relative faintness of HH 34N probably arise from absorption by the intervening ambient cloud material.

BMR acquired long-slit spectra across the HH 34 working surface and the visible jet that show complex Hα and [S II] λλ6716, 6731 emission line profiles. Such long-slit spectra can efficiently map the kinematics of the linear jet, but they are much less efficient for spatially resolved kinematic mapping of extended emission-line sources, such as the working surface HH 34. BMR estimated radial velocities and electron densities along nine long-slit positions across the bow shock. The Hα line profiles are double-peaked in some of the brighter knots, with components at -120 km s^{-1} and -30 km s^{-1}, while the [S II] intensity peaks in one knot at -150 km s^{-1} and -85 km s^{-1}. From low-resolution spectrograms, they measured electron densities in the bow shock as high as 740 cm^{-3} in one knot, but more typically ~ 300 cm^{-3}. Their results demonstrate that the [S II] and Hα emission distributions are inhomogeneous.

The long-slit spectra by Heathcote & Reipurth (1992; hereafter HR92; see also Reipurth 1989a) show continuous line emission from the jet source to the bow shock HH 34. Their [S II] echelle spectrogram shows a complex velocity structure with multiple peaks in both the jet and HH 34. However, these authors note the general trend in their spectrogram of a monotonically increasing velocity from the source to the bow shock. Narrow-band [S II] and Hα images at several epochs suggest that tangential velocities in the visible jet are ~ 200 km s^{-1}. They find the puzzling results that the tangential and radial velocities in the bow shocks HH 34 and HH 34N are $\sim 50\%$ larger than in the jet.

Reipurth & Heathcote (1992) have subtracted [S II] and Hα images of HH 34 to reveal a small region of strong [S II] emission that is embedded in an outer envelope of Hα emission in the HH 34 working surface. The [S II] region lies directly along the jet axis and coincides with knot F, as labeled by Reipurth et al. (1986). They suggest that this is the Mach disk in HH 34. Our results in § 4.2 support this suggestion. They also report evidence for the existence of multiple bow shocks (in addition to HH 34) in the approaching lobe, that were ejected at intervals of ~ 400 yr.

2.2. *Fabry-Perot Observations and Reductions*

Astronomical application of imaging Fabry-Perot (F-P) spectrometers has been described in detail by Atherton et al. (1982). Briefly, when used in a parallel beam, incident light undergoes destructive interference between the coated surfaces in the F-P etalon such that a single wavelength of light is passed along the optical axis. The wavelength passed can be altered by varying the gap between the coated surfaces. Due to the variable distance from the optical center of the etalon to each pixel on the (flat) detector, there is a velocity curvature across the field of view. Thus the images are not strictly monochromatic; the wavelength at each pixel is a function of both the etalon gap and the distance off-axis. The velocity curvature is well-defined and can be removed (called "phase correcting") by calibrating the radial wavelength dependence with an arc-lamp emission line of known wavelength. The calibrating emission line is a diffuse monochromatic light source that is imaged as a ring centered at the on-axis position and with radius determined by the etalon gap and wavelength of light.

The F-P data were acquired by taking a sequence of exposures at etalon gaps which sampled a selected emission line from the object at regular velocity intervals. Line widths in HH 34 are typically a couple of hundred km s^{-1} which we have sampled at ~ 15–20 km s^{-1} intervals. The images were stacked into a "velocity data cube," and then phase corrected to produce a grid of spectral line profiles across the emission source. A spectrophotometric standard star was observed over the same wavelength region to obtain absolute fluxes for each line profile.

The Rutgers/CTIO CCD-based imaging Fabry-Perot was used on the CTIO 4 m telescope in 1989 November and 1991 February to obtain full spatial and partial kinematic sampling of the HH 34 system in the [O III] λ5007, Hα and [S II] λλ6716,

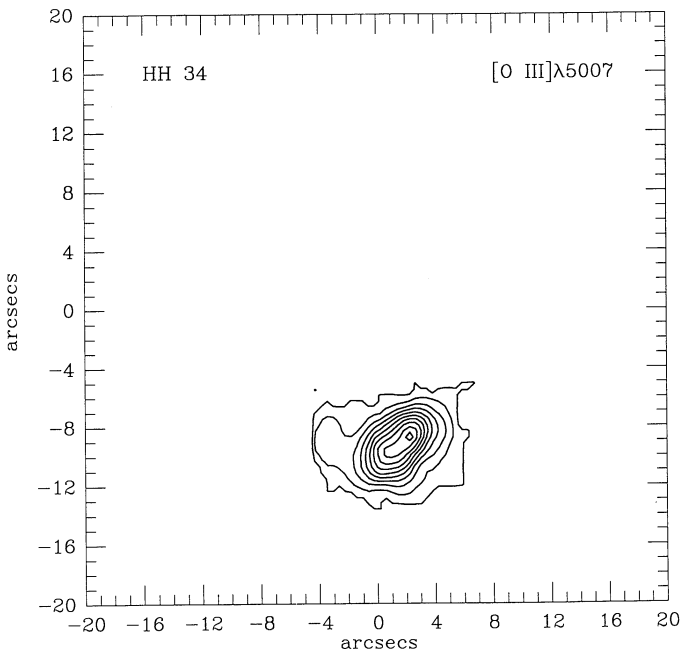

FIG. 1*a*

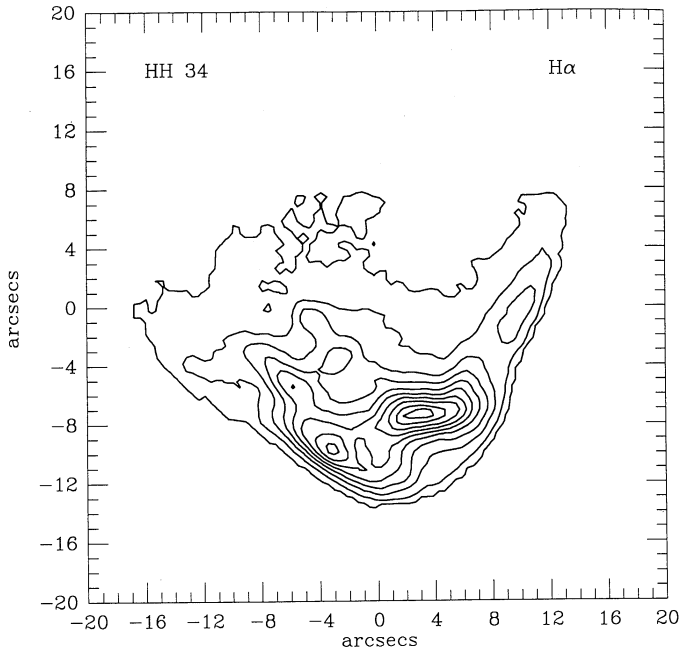

FIG. 1*b*

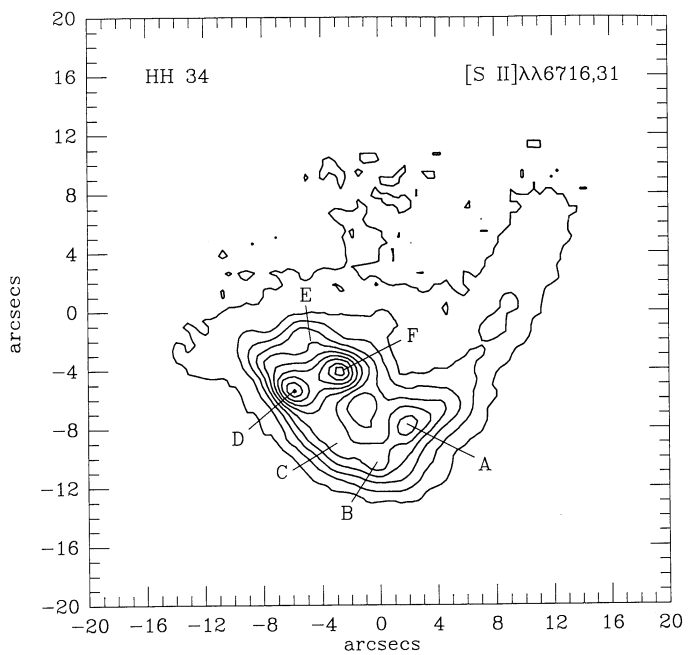

FIG. 1*c*

FIG. 1.—Images of the working surface HH 34 in the (*a*) [O III] λ5007, (*b*) Hα, and (*c*) [S II] (λ6716 + λ6731) emission lines, summed over the individual velocity images for each line. Each image has been rotated by ~13° counterclockwise to align the approximate axis of symmetry with the *y*-axis. The jet axis is displaced approximately −3″ relative to the center. North is to the top, and east is to the left, although these directions are not precisely aligned with the *x*-*y* axes. In all plots, contour levels are set to 10%, 20%, 30%, 40%, 50%, 60%, 70%, 80%, 90%, and 97% of the maximum value. The peak reddening-corrected luminosities (§ 3.3) are 4.1×10^{28} ergs s^{-1}, 8.1×10^{28} ergs s^{-1}, and 4.5×10^{28} ergs s^{-1} for [O III], Hα and [S II], respectively. Note that these images result from summing over only a partial sampling of each emission line profile, so these peak luminosities underestimate those that would be obtained through narrowband images which completely sample the emission lines.

6731 emission lines. The TI2 chip was used in the first run and the TEK4 chip in the second. In both cases the image scale was ~0.″4 $pixel^{-1}$, providing a field of diameter 2.′5. The etalon had a free spectral range (FSR) of 18 Å (~900 km s^{-1}) and a FWHM resolution of 0.7 Å (~35 km s^{-1}). Narrow-band [O III], Hα, and [S II] filters were placed in the collimated beam to pass only a few spectral orders. The central wavelengths (FWHM bandpasses) for the [O III], Hα and [S II] filters were 4993 Å (38 Å), 6563 Å, (12 Å), and 6737 Å (76 Å), respectively. We obtained the Hα and [S II] data sets in the first run with the TI chip, and the [O III] data in the second run with the TEK chip. The exposure time for nearly all of the images was 900 s, yielding a typical signal-to-noise level of 10–20 for images with considerable emission in the working surface, and a monochromatic flux limit of $\sim 1 \times 10^{-17}$ ergs s^{-1} cm^{-2} $Å^{-1}$ $arcsec^{-2}$. The images were bias-subtracted using standard routines in IRAF and corrected for atmospheric extinction using standard CTIO extinction coefficients.

Atherton et al. (1982) and Bland & Tully (1989) detail the procedures for flat fielding and phase correcting Fabry-Perot data sets. The widths of our order separation filters generally exceeded the FSR of the etalon, so that the "white-light" flat fields passed light from several spectral orders. We obtained a flat field at every etalon gap setting at which data were taken, but because they contained light from several overlapping orders, we normalized each individual flat field and corrected for the filter transmission after phase correcting.

We removed rings of ambient line emission that arose from the gas surrounding HH 34. The radius and width of each ring was measured, then a median profile binned across the ring was subtracted in a circle centered at the on-axis position. In general, ring removal was complicated by intensity variations around the ring. Fortunately, the ambient emission contaminated the jet and bow shock emission in only a few images. In these instances, we assigned an additional uncertainty of $\sim 10\%$ to the flux measurements.

The data cubes were then phase corrected to stacks of monochromatic images using a Ne-Ar comparison lamp. The dispersion relation, calibrating the change in on-axis wavelength as a function of etalon setting, and velocity zero-point were verified by measuring radii of the narrow emission rings that arise from diffuse [O III], Hα, and [S II] emission in the HH 34 region at a heliocentric velocity $\approx +25$ km s^{-1} (see § 4.1.1). Our limited sampling over a large range in velocity, combined with temperature drifts in the etalon through a given set of observations, led to uncertainties of about ± 10 km s^{-1} between the extreme regions of the working surface. The monochromatic images were then stacked into velocity data cubes using custom IRAF routines. The spectophotometric standard star LTT4364 was observed to convert ADU to absolute fluxes (Hamuy et al. 1992).

By observing at the same velocity in each line of the [S II] doublet, we were able to obtain complete spatial maps of the [S II] λ6716/λ6731 line ratio and to add each velocity pair to map the total [S II] emission. Over a wide temperature range, *the line ratios map electron densities at each velocity for every point in the images. Thus, we can infer electron densities at specific locations in the volume delineated by the working surface.* We were also able to map the [S II]/Hα ratio at each [S II] velocity. We excluded the background below $\sim 2\,\sigma$ of the mean sky when ratioing images, to restrict our subsequent analysis to bright regions.

3. RESULTS

In this section we present our results for the HH 34 bow shock and Mach disk. We have summed our velocity images in each data cube in Figure 1 which shows the integrated [O III], Hα, and [S II] intensity maps of the HH 34 working surface. Several emission knots previously identified by Reipurth et al. (1986) are marked in the [S II] frame. To ease comparison with the models (§ 4.1.4), we rotated each image counterclockwise by $\sim 13°$ in all the figures, to align the approximate axis of symmetry in the data along the vertical axis.

3.1. *Line Profiles across the HH 34 Working Surface*

Fabry-Perot spectrophotometers provide spatially complete maps of extended emission sources, and our [O III], Hα and [S II] data cubes have sampled the emission profiles at each point in HH 34. We can present the velocity data cubes either as a set of monochromatic images, or as a set of spectra on a spatial grid. We prefer the latter presentation (Fig. 2) because it is easier to compare the data with the models when we use grids of spectral profiles. Our data cubes consist of 13 velocity images in [O III] λ5007 that covered a range from -200 to -20 km s^{-1} at ~ 15 km s^{-1} intervals, 15 velocity slices in Hα from -200 to $+80$ km s^{-1} at 20 km s^{-1} intervals, and 11 velocity pairs in each line of the [S II] λλ6716, 6731 doublet from -160 to $+40$ km s^{-1} also at 20 km s^{-1} intervals. Our velocity sampling covered most of the emission—the profiles go to zero except in the [S II] data cube in the region of knots D, E, and F. Summing up all of the emission from each line produces images that are nearly identical to the emission-line images of BMR (Fig. 1).

3.2. *Electron Densities and Excitation Conditions*

Our Fabry-Perot observations of HH 34 enable us *for the first time* to measure line ratios at each spatial position as a function of velocity. Hence, we can determine how the electron density varies with position and velocity by using the [S II] λ6716/λ6731 ratio to measure the electron density (McCall 1984). Our estimates of the "average" electron densities in HH 34 (found by ratioing the *velocity-integrated* [S II] λ6716 and [S II] λ6731 emission at each point) agree well with the values reported by BMR. However, these electron densities are derived from line fluxes which are averaged along the line of sight through the working surface (for an optically thin nebula). The electron densities show large variations as a function of velocity compared to the average values. For example, BMR report that $n_e \approx 740$ cm^{-3} in the bright knot A in the working surface. It is evident from the Hα and [S II] spectral grids (as well as Figure 11 of BMR) that the profiles in this region are double-peaked. Figures 3*a* and 3*b* (Plate 6) map the high-velocity [S II] emission intensity, together with the electron densities. Note the absence of the bow shock wings and how the bow shock and putative Mach disk are almost completely separated. The electron densities for the high-velocity component in the region of knot A exceed 1300 cm^{-3} but are more typically ~ 1100 cm^{-3}. Electron densities for the low-velocity emission in knot A are 300–400 cm^{-3}. By contrast, the electron densities in Figure 3 for knots D, E, and F are an order of magnitude lower than at the apex of the bow shock.

Figure 4 (Plate 6) maps the average [S II]/Hα ratios across HH 34. Very low values (gray and blue) are confined to a thin ribbon toward the edge of the bow shock, whereas the highest values (red and lavender) are found away from the forward edge of the bow shock, especially in the region of the putative Mach disk. The strong gradient in the [S II]/Hα line ratio across the western wing could have several explanations. It might arise from a resolved postshock cooling distance, or we might be seeing emission from shocked ISM gas toward the leading edge and reionized, backflowing jet material away from the edge, with the two regions separated by a contact discontinuity. The possibility that the postshock cooling distance is resolved was discussed by BMR, who noticed an obvious spatial separation between the [S II] and Hα emission in the wing, and was modeled by Raga & Binette (1991). We favor this explanation. The strong Hα emission along the leading edge would arise from collisional excitation of the ambient gas, while the steep gradient to predominantly [S II] emission tracks radiative cooling in the recombination zone as the temperature falls from $\sim 10^4$ K to 5000 K. In this case, the cooling distances may be on the order of several arcseconds ($\sim 10^{16}$ cm

PLATE 6

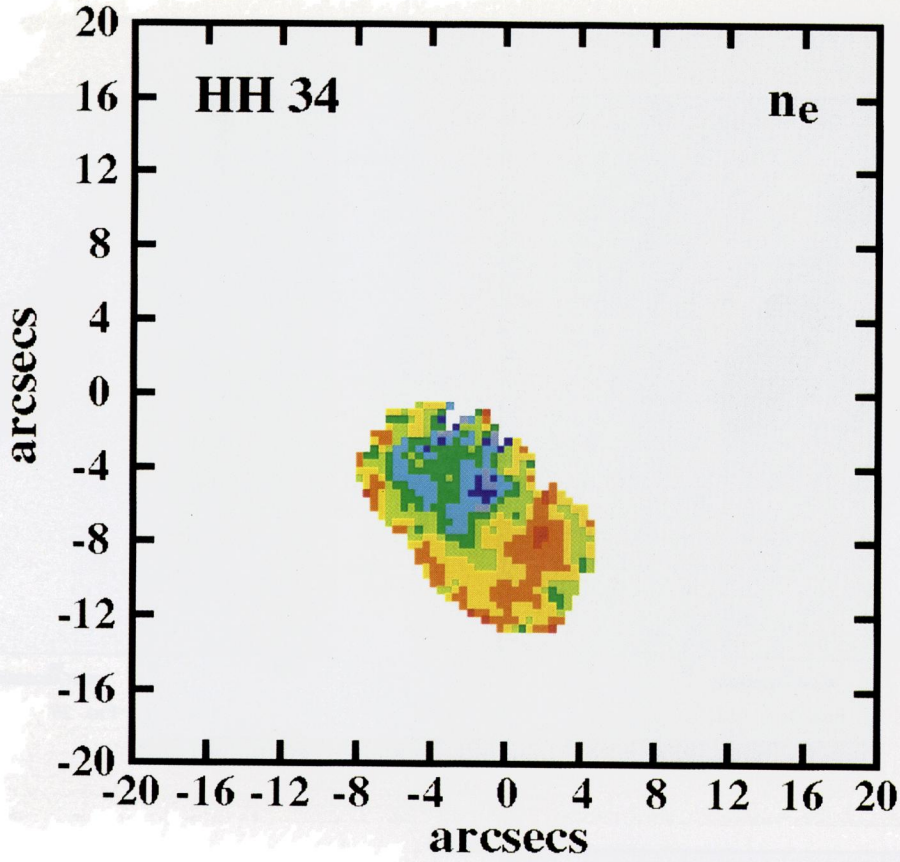

FIG. 3*b*

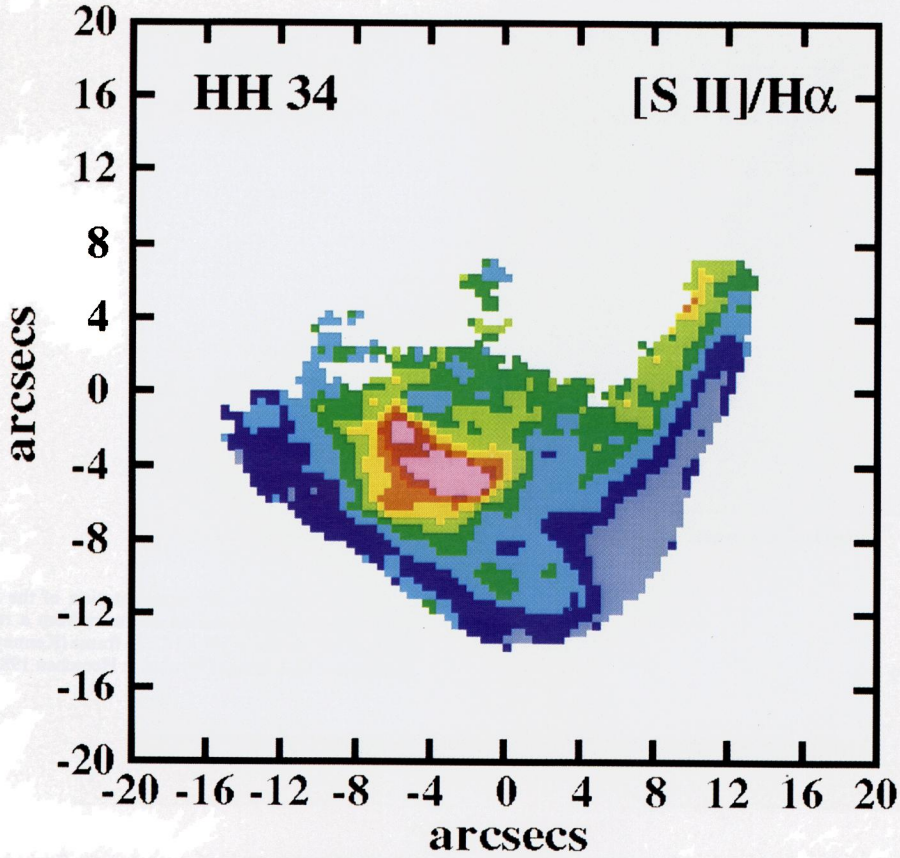

FIG. 4.—Map of average [S II]/Hα ratios. The colors correspond to the following values: dark gray: 0.1 < [S II]/Hα < 0.2; blue: 0.2 < [S II]/Hα < 0.35; light blue: 0.35 < [S II]/Hα < 0.5; dark green: 0.5 < [S II]/Hα < 0.65; light green: 0.65 < [S II]/Hα < 0.8; yellow: 0.8 < [S II]/Hα < 0.95; orange: 0.95 < [S II]/Hα < 1.1; red: 1.1 < [S II]/Hα < 1.3; lavender: 1.3 < [S II]/Hα < 1.5.

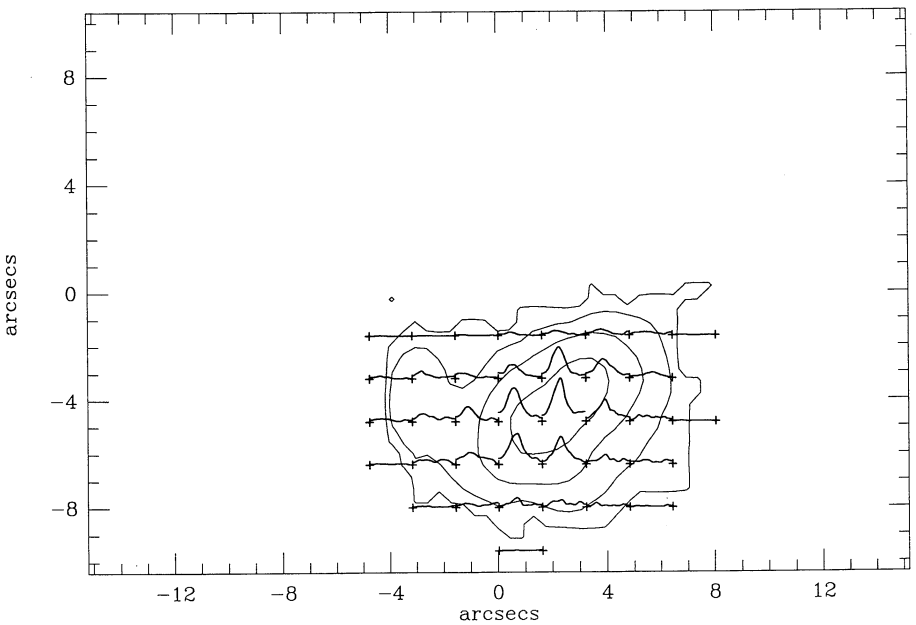

FIG. 2*a*

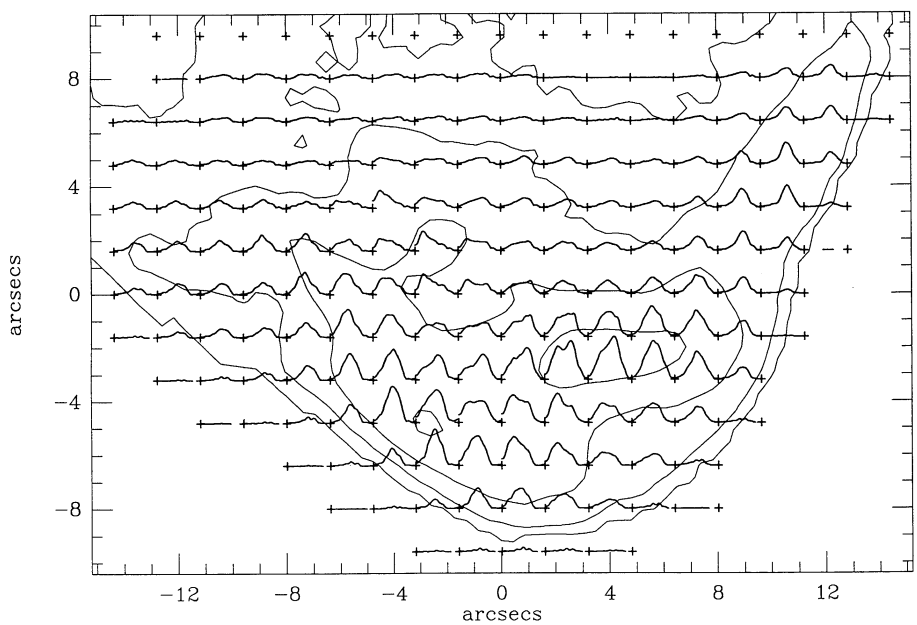

FIG. 2*b*

FIG. 2.—Spectral grids for the (*a*) [O III] λ5007, (*b*) Hα, and (*c*) [S II] (λ6716 + λ6731) emission lines. All spectra have been interpolated (linearly) to 5 km s^{-1} intervals between observed velocities and smoothed by a Gaussian with FWHM equal to our instrumental resolution (35 km s^{-1}). To reduce confusion only four underlying contours of the images from Fig. 1 are drawn, at 10%, 20%, 40%, and 80% of the maximum value. Each spectrum is the sum of 4 × 4 pixels (to approximate our seeing). The velocity limits of the spectra for each line are: [O III] from −200 to −20 km s^{-1}, Hα from −200 to +80 km s^{-1}, and [S II] from −160 to +40 km s^{-1}, with bluer wavelengths to the left. The spectra are normalized to the maximum of the highest peak in each grid to preserve the relative intensities as a function of position across the working surface. Note the multipeaked profiles through the middle of the Hα and [S II] grids, and the high-velocity emission in the region of knots D, E, and F that we identify with a Mach disk (§ 4.2.1). [O III] appears only at the apex of the bow shock and shows that the bow shock and Mach disk have very different line excitation in addition to having very different kinematics.

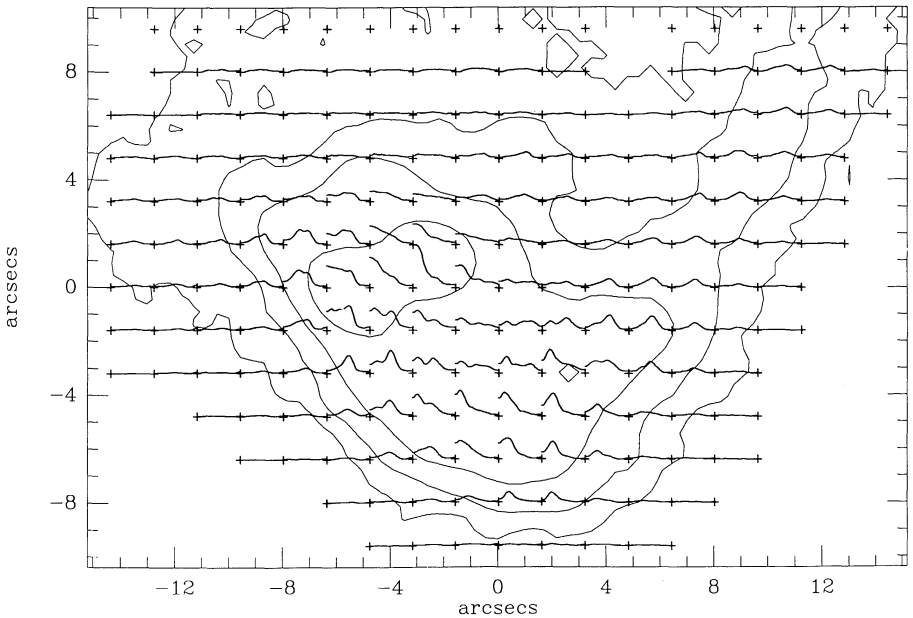

FIG. 2c

at a distance of 460 pc),[2] which are large compared to those predicted in planar shock models (e.g., Raymond 1979; Shull & McKee 1979). Raga & Binette (1991) present one-dimensional shock models with relatively low shock velocities (≤ 50 km s^{-1}), low preshock density (~ 10 cm^{-3}) and partial preionization, that produce a stratified postshock cooling region and may account for the spatial separation of the [S II] and Hα emission in HH 34. We further note that (1) the postshock gas may be carried much farther downstream than the planar shock models indicate because the relatively larger parallel velocity component is preserved across the shock, although this effect requires a detailed two-dimensional treatment to fully evaluate the effects of the curved bow shock surface on the postshock gas propagation; and (2) at these shock velocities, even a modest preshock magnetic field (~ 10 μG) extends the cooling region by a factor of 10.

3.3. *Fluxes and Reddening Correction*

Absolute fluxes we derived from our HH 34 data are somewhat uncertain because the filters available to us passed more than a single spectral order of the continuum of our standard star LTT 4364 (see § 2.2). The contamination in the Hα filter was least because its transmission profile was only slightly wider than the FSR of the etalon. We quantified the degree of order overlap for the Hα filter and corrected the standard star flux for the light contamination. By convolving the filter trans-

[2] We estimate the cooling distance roughly along the vector V_2 drawn in Figure 1 of Hartigan, Raymond & Hartmann 1987 and *not* perpendicular to the shock front, as previous estimates have done. For gas entering a planar shock at an oblique angle, the postshock perpendicular velocity component nearly comes to rest with respect to the shock front after a cooling time while the conserved parallel velocity component carries the gas parallel to the shock surface. In this case, the parallel component of the velocity will not affect the spatial separation of the [S II] and Hα emission, and the separation perpendicular to the shock surface effectively measures the one-dimensional cooling distance for a shock with velocity $V_\perp$. However, the curvature of the bow shock may alter the velocity field and postshock spatial emission distribution compared to the oblique planar case. The velocity fields predicted in two-dimensional hydrodynamical simulations of bow shocks (J. Blondin, private communication) suggest that the postshock gas is not carried downstream exactly parallel to the shock surface through which it entered. The resolution of this issue rests on solving the two-dimensional (or three-dimensional) hydrodynamical problem with proper treatment of ionization, radiative transfer and magnetic fields.

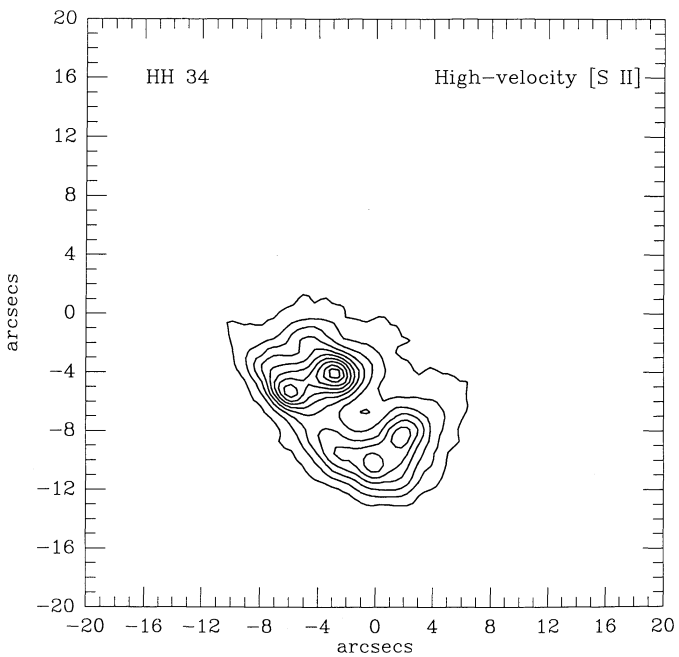

FIG. 3a

FIG. 3.—High-velocity [S II] intensity and electron density maps. (*a*) The intensity contours are set to the same relative values as in Fig. 1 except that the peak luminosity is $\sim 4.1 \times 10^{28}$ ergs s^{-1}. (*b*) The colors correspond to the following electron densities: dark gray: $n_e < 50$ cm^{-3}; blue: $50 < n_e < 100$ cm^{-3}; light blue: $100 < n_e < 150$ cm^{-3}; dark green: $150 < n_e < 200$ cm^{-3}; light green: $200 < n_e < 400$ cm^{-3}; yellow: $400 < n_e < 650$ cm^{-3}; orange: $650 < n_e < 1100$ cm^{-3}; red: $1100 < n_e < 1400$ cm^{-3}.

mission profile with the periodic Airy function of the etalon, we estimated 15% ± 5% contamination by the neighboring orders at Hα to the observed standard star flux. We then applied the flux calibration to the [O III] and [S II] wavelength regions, correcting for the wavelength dependence of the detector responses as measured at CTIO. The [O III] λ5007 flux was corrected by 15% due to the lower detector response relative to Hα, while the [S II] fluxes were not changed. We used a TEK rather than a TI CCD for the second run, so we observed at several redundant velocities in Hα in the second run to register the relative responses of the two detectors. An additional uncertainty of ~5% in the flux calibrations results from night-to-night and run-to-run variations in the atmospheric transparency.

We summed the line profiles from the entire working surface for each of the lines we observed to obtain the total line fluxes from HH 34. The observed integrated [O III] λ5007 line flux is $\sim 1.6 \times 10^{-14}$ ergs s^{-1} cm^{-2}. As explained in § 4.1.2, we attribute all [O III] flux to post–bow shock emission. The integrated fluxes for Hα and [S II] over the entire working surface include contributions from the bow shock and the Mach disk. The observed Hα flux is 3.6×10^{-13} ergs s^{-1} cm^{-2}, and the combined [S II] λλ6716, 6731 flux is 1.9×10^{-13} ergs s^{-1} cm^{-2}. The error in measuring the total amount of emission from the working surface is on the order of ±10%, with additional error in the reported fluxes arising from uncertainties in the flux calibration (±15%).

Reddening introduces the largest uncertainty in converting to absolute fluxes. As evident by the relative faintness of the northern bow shock HH 34N (see BMR), the extinction may differ drastically over spatial scales ~1′. We have estimated the reddening from two long-slit spectra of HH 34 obtained for another program. The spectra were obtained at the same slit position as the echelle spectrum shown in HR92. The slit was 2″ wide and passed through the stellar source and knots F and C in HH 34. We extracted the spectra from the apex of the bow shock where [O III] λ5007 emission was evident, including knot C, and estimated the reddening from the Hα/Hβ line ratio as follows. The shock velocity must be $\gtrsim$100 km s^{-1} to get significant [O III] emission and, in this domain of shock velocities, the predicted Hα/Hβ ratio is ~3.0 for equilibrium preionization conditions (see, for example, Hartigan, Raymond, & Hartmann 1987; hereafter HRH). The observed Hα/Hβ ratio is 4.4 ± 0.2 at the apex, where the error is the standard deviation of the values derived independently from the two exposures. Using the standard reddening law described by Cardelli, Clayton, & Mathis (1989), with $R_V = 3.1$, adjusting the Hα/Hβ ratio to 3.0 requires $A_V = 1.26 \pm 0.11$ and $E(B-V) = 0.41 \pm 0.04$. This $E(B-V)$ agrees with that found by Solf, Böhm, & Raga (1988) using the blue and near-IR [S II] lines for the nearby HH 1 complex. The corrected fluxes across the entire working surface for [O III] λ5007, Hα, and [S II] λλ6716, 6731 are then 5.8×10^{-14} ergs s^{-1} cm^{-2}, 9.3×10^{-13} ergs s^{-1} cm^{-2} and 4.9×10^{-13} ergs s^{-1} cm^{-2}, respectively, ±20% due to uncertainties in $E(B-V)$ and the flux calibration.

4. DISCUSSION

4.1. *A New Bow Shock Model for HH 34*

4.1.1. *Inclination to Line of Sight*

HH 34 is an excellent laboratory for studying working surface interactions and to compare theoretical models of working surface dynamics. The first parameter necessary for a useful comparison is the inclination angle to the line of sight of the blueshifted jet/bow shock system. HR92 report tangential velocities in the brightest jet knots ≈200 km s^{-1} (using a distance of 460 pc to the system and assuming that the measured velocities in the jet represent the true flow speed). The heliocentric radial velocity of the brightest knots is ≈ −80 km s^{-1} (HR92, BMR). However, we are interested in the velocity relative to the exciting star. From ^{12}CO maps of the region, Reipurth et al. (1986) obtained a velocity of $V_{LSR} \approx +8.6$ km s^{-1}, or ~ +26 km s^{-1} heliocentric, for the molecular cloud complex around HH 34. We also measured the ambient emission in our data at $V_{hel} \approx +25 \pm 5$ km s^{-1}, in agreement with that shown in the HR92 spectrogram. Therefore, we adopt +25 km s^{-1} for the systemic radial velocity of the system. The relative radial velocity of the jet knots to the ambient medium becomes ~ −105 km s^{-1}. We infer an inclination angle to the line of sight of $\phi \sim 62°$ with a probable error of several degrees from uncertainties in the tangential- and radial-velocity measurements, the distance to HH 34 (±20%; HR92), and whether the emission in the jet knots does in fact represent the true flow speed. HR92 have also measured the tangential and radial velocities for knot F in the working surface and find a value of $\phi = 59 \pm 1°$, in agreement with the jet value. Therefore, we adopt $\phi = 60°$ for the HH 34 system.

4.1.2. *Determination of Shock Velocity and Bow Shock Shape*

The bow shock velocity for HH 34 is the most important physical parameter to constrain. Once it is determined, our strategy is to model the bow shock emission using the observed bow shock shape, new shock models, and the geometry described in HRH. Then we analyze the deviations of our data from the model, which may arise from Mach disk emission, dynamical instabilities, and asymmetries in the environment.

With a given shock velocity, ambient pressure, elemental abundances, preshock ionization, magnetic field, and bow shock geometry, the models predict the spatial emission distribution, line profiles, line widths, line fluxes, and line ratios. Conversely, by inferring a three-dimensional geometry from the observed, projected, bow shock shape, and inclination to the line of sight, and measuring the spatial emission distribution, line profiles and line widths, we can deduce the shock velocity. One of the more curious observations of HH 34 that the models must explain is the large velocities, both radial and tangential, combined with a relatively low ionization state. (Even more drastic examples of this situation occur in, e.g., HH 11, see Solf & Böhm 1987; and HH 111, see Reipurth, Raga, & Heathcote 1992 and Morse et al. 1992.) Tangential velocities in the working surface ~285 km s^{-1} are reported by HR92, while the measured FWZI line widths from our data and those of previous investigators exceed 200 km s^{-1}. Conversely, higher ionization line species (such as [O III])—which would be expected to dominate the bow shock emission if the shock velocity was so high—have been observed only at the apex of the bow shock, while relatively lower ionization species, such as Hα and [S II], are the dominant emitters from the apex back into the wings of the bow shock.

HRH describe how to estimate the shock velocity from the FWZI of the emission lines and find $V_S \approx$ FWZI for a large range of inclinations. However, if the shock velocity indeed exceeds 200 km s^{-1}, then the [O III] emission would extend well into the bow shock wings, which it does not. Hence, there must be a line broadening mechanism (of ~50 km s^{-1}) in

addition to thermal broadening in HH 34. We instead use the [O III] λ5007 emission distribution—given the bow shock shape and inclination—to deduce the shock velocity. The [O III] emission is confined exclusively to the apex of the bow shock (see Fig. 2) and so arises from ambient gas that has been accelerated through the bow shock.

We fit the observed shape of HH 34 from the summed Hα and [S II] images with a simple parabola,

$$Z_0 = \alpha_0 R_0^2 , \tag{1}$$

where Z_0 and R_0 are measured in arcseconds along the axis of symmetry and perpendicular to the axis, respectively, and $\alpha_0 \approx 0.09$. The uncertainty in α_0 is $\sim 5\%$. Then from Hartigan, Raymond, & Meaburn (1990; eq. [A9]), the true shape of the bow shock is

$$Z = \frac{\alpha_0}{\sin \phi} R^2 , \tag{2}$$

where $\phi = 60°$ is the viewing angle of the observer. For equilibrium preionization, the [O III] λ5007 begins to emit at shock velocities $\gtrsim 100$ km s^{-1} (see HRH). Therefore, at the point in the wings of the bow shock where the [O III] emission ceases, the perpendicular shock velocity $V_\perp = V_c \approx 100$ km s^{-1}. The width of the [O III] emission distribution perpendicular to the axis of symmetry is $2R_c \approx 9\farcs5 \pm 1\farcs0$ (see Fig. 1). This value for R_c ignores seeing effects but also assumes that we measure very faint emission, errors that will tend to cancel. Note that R_c is independent of the viewing angle ϕ. Now,

$$\cot \xi = \frac{dR}{dZ} = \frac{\sin \phi}{2\alpha_0}\left(\frac{1}{R}\right), \tag{3}$$

where ξ is the angle between the axis of symmetry and the normal to the bow shock (see Fig. 1 of HRH). We find the bow shock velocity, V_S, using the identity

$$\frac{1}{\cos \xi} = \left(1 + \frac{1}{\cot^2 \xi}\right)^{1/2} \tag{4}$$

so that

$$V_S = \frac{V_\perp}{\cos \xi} = V_\perp\left(1 + \frac{4\alpha_0^2}{\sin^2 \phi} R^2\right)^{1/2} . \tag{5}$$

Substituting the critical values $V_\perp = V_c \approx 100$ km s^{-1} and $R = R_c \approx 4\farcs8$ in equation (5), we find $V_S \approx 140 \pm 20$ km s^{-1}, where the error accounts for the uncertainties in α_0, R_c and ϕ. As described in the following subsections, using this shock velocity in our bow shock model is reasonably successful at predicting the observed line profiles. Other investigators (BMR, 120–170 km s^{-1}; HR92, 160 km s^{-1}) have made similar estimates for the bow shock velocity in HH 34.

4.1.3. *Planar Shock Models for the HH 34 Bow Shock*

The planar shock models that we used to model the HH 34 bow shock emission are detailed in Raymond (1979), Cox & Raymond (1985), and HRH. Our approach is to model the bow shock emission by interpolating among a series of planar shock models (Hartmann & Raymond 1984; HRH). The variation of the perpendicular velocity, $V_\perp$, across the bow shock requires a grid of models closely spaced in shock velocity. Hence, planar models were calculated at 10 km s^{-1} intervals over the range 40–140 km s^{-1}.

We have determined the preshock density, n_0, from the observed Hα flux at the apex of the bow shock, where [O III] emission is present and the shock velocities are reasonably well known. The preshock density can be found from the Hα flux using the two relations:

$$L_{H\alpha} = n_0 V_{ap} \sigma_c \left(\frac{hc}{\lambda}\right) f_{H\alpha} , \tag{6}$$

where $L_{H\alpha}$ is the observed Hα luminosity at the apex, n_0 the preshock density, V_{ap} the effective shock velocity of the emitting region, σ_c the cross sectional area of the emitting region, hc/λ the photon energy at $\lambda = 6563$ Å, $f_{H\alpha}$ the number of Hα photons per H atom; and

$$L_{H\alpha} = 4\pi d^2 F_{H\alpha} , \tag{7}$$

where d is the distance to HH 34, and $F_{H\alpha}$ the Hα flux observed at the apex. Thus,

$$n_0 = \frac{4\pi d^2 F_{H\alpha}}{V_{ap} \sigma_c f_{H\alpha}} \left(\frac{\lambda}{hc}\right) . \tag{8}$$

The reddening-corrected Hα flux observed in the region subtended by the [O III] emission is $F_{H\alpha} \approx 2.3 \times 10^{-13}$ ergs s^{-1} cm^{-2}. The effective shock velocity $V_{ap} \approx 120$ km s^{-1} is, in this case, the mean shock velocity weighted over the area of the emitting surface. The emitting area $\sigma_c = \pi R_c^2 = 72.4$ arcsec$^2 \approx 3.4 \times 10^{33}$ cm^2, with R_c as defined in the previous section, and using a distance $d = 460$ pc to HH 34. Finally, $f_{H\alpha} \approx 0.75$. Because we found that $f_{H\alpha}$ remains nearly constant for shock velocities ≈ 120 km s^{-1} for a variety of preionization conditions and magnetic field strengths, we used the Hα rather than the [O III] λ5007 flux to calculate the preshock density. The value of f_{5007} varied significantly over a small range in shock velocities and preionization conditions. In addition, the Hα flux is less affected by reddening than the [O III] flux. Substituting these values in equation (10), the predicted preshock density derived from the observed Hα flux $n_0 \approx 65 \pm 20$ cm^{-3}, where the 30% error accounts for our estimated uncertainties in R_c, $f_{H\alpha}$, the absolute flux, the distance to HH 34, and the effective shock velocity.

HR92 suggest that faint emission just in front of the HH 34 bow shock (at a radial velocity of -85 km s^{-1} relative to the source) is from preionized gas. We have estimated the ionization state of the preshock gas using the procedures outlined by Raymond, Hartigan, & Hartmann (1988) in their study of HH 2A′. Briefly, the calculation predicts the preshock ionization of H as a function of $V_\perp$ given a bow shock shape and n_0. In general, the assumption of local equilibrium preionization breaks down because the preshock gas in the bow shock wings is exposed to ionizing radiation from regions of higher effective shock velocity nearer to the apex. Raymond et al. found for HH2A′ that with the severe curvature of the bow shock, the preshock gas is less ionized near the apex and more ionized in the wings than with local equilibrium preionization. The curvature of the HH 34 bow shock is much less severe than for HH2A′, so that the departure from local equilibrium preionization is not very pronounced (Fig. 5). There is, however, significant partial preionization in the bow shock wings resulting from the radiation field produced near the apex. But the calculated neutral fractions are not so different from the equilibrium values that it invalidates the assumptions we made about the cutoff shock velocity at the extremes of the [O III] λ5007 emission distribution when we derived a bow shock velocity of 140 km s^{-1} (§ 4.1.2).

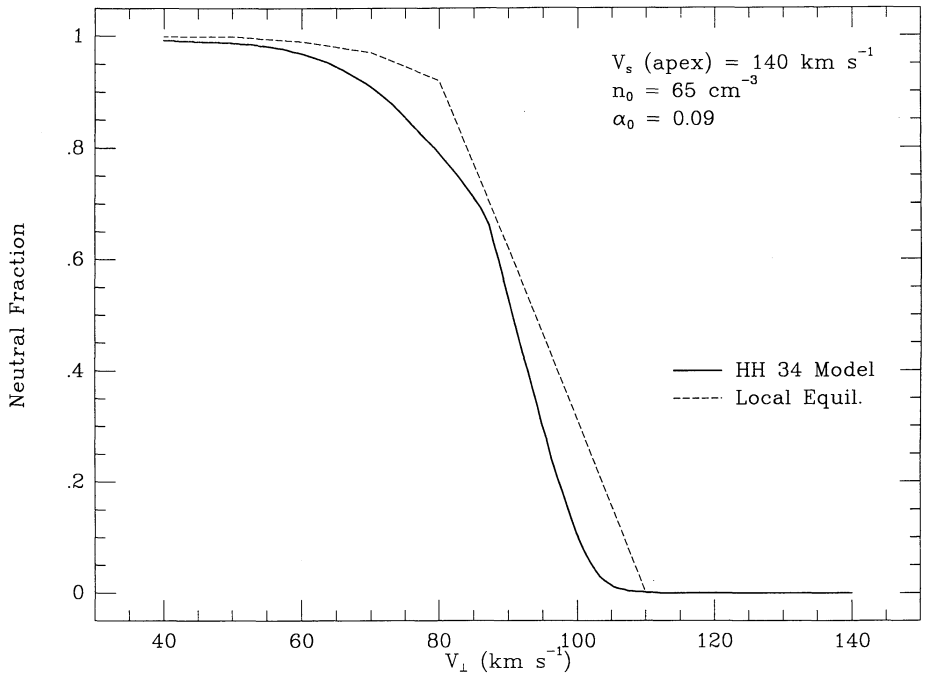

FIG. 5.—The hydrogen neutral fraction as a function of perpendicular shock velocity for gas encountering the HH 34 bow shock. The calculated neutral fractions are shown as the solid line, and local equilibrium preionization neutral fractions as the dashed curve.

Emission from [O III] strongly depends on the preshock ionization over the range in shock velocities ~80–120 km s^{-1} (Cox & Raymond 1985). A similar calculation of the preionization for a bow shock velocity of 160 km s^{-1} at the apex predicted that the preshock gas was fully ionized down to $V_\perp \approx 80$ km s^{-1}. In this case [O III] λ5007 emits as strongly as Hα down to $V_\perp \approx 80$ km s^{-1}, and the model produces [O III] emission in the bow shock wings that is not observed. For this reason, we conclude the bow shock velocity must be somewhat less than 160 km s^{-1}.

The ionization balance between He^0 and He^+ was assumed to be the same as the hydrogen neutral-to-ionized ratio. For local equilibrium preionization, helium is doubly ionized only for shock velocities $\geq$110 km s^{-1} (see HRH). Since the calculated preionization is basically identical to the equilibrium curve for these shock velocities (Fig. 5), we used the equilibrium preionization values for He^{++} from HRH in our models. We chose small step sizes in our computations to adequately sample the postshock temperatures near 10^4 K where the cooling gas becomes optically thick to Lyman-continuum photons.

We fixed the logarithmic abundance ratios in the models for H:He:N:O:Ne:S:Ar:Fe:Ni to values of 12.00:11.00:7.72:8.49:7.60:6.97:6.41:6.43:5.15 as derived by Osterbrock, Tran, & Veilleux (1992) for the Orion Nebula region. Note that these abundances are metal poor relative to the "cosmic" values (Allen 1973) and account for the low line ratios (e.g., [S II]/Hα, [O III]/Hα, [N II]/Hα) observed by us, Reipurth et al. (1986), and BMR.[3] The abundances for C:Mg:Si:Ca were set to the "cosmic" values of 8.52:7.42:7.52:6.30. The preshock temperature was always taken to be 10^4 K. A radiative transfer parameter R_{max} (Cox 1972; Raymond et al. 1988) was taken to be 1, appropriate for the nonplanar geometry of a bow shock. Calculation of the emission-line fluxes was terminated either when the gas temperature cooled below 1000 K or the cooling time exceeded 800 years, approximately the maximum dynamical lifetime of the bow shock (HR92).

An interesting aspect of our new shock models is the inclusion of an ambient magnetic field, B_0. Models for HH objects (e.g., in HRH) have tended to assume $B_0 = 0$. We were able to constrain B_0 by comparing the compression across the HH 34 bow shock to the compression predicted by shock models computed over a range in B_0 from 0.1–100 μG. We define the compression, X, as the ratio of the postshock electron density, as measured by the [S II] λ6716/λ6731 ratio, to the preshock density, n_0, in both the data and the models. Figure 6 displays the results. The HH 34 data were taken from electron densities measured in the individual velocity images as a function of position and velocity along the western wing of the bow shock. The individual measurements are marked by the open boxes and are connected by the solid line. The compressions measured in the models are shown by the dotted curves. (Some values for X are <1 because the [S II] line ratio measures electron densities, which, for low shock velocities and large magnetic fields, do not trace the true gas density.) The error bars assigned to the data points in the top plot account for the statistical uncertainties in the measured electron densities. These errors increase toward lower shock velocities due to a decrease in the signal-to-noise ratio of the data toward the extremes of the bow shock wing. The error bars in the bottom plot account for our uncertainty in the preshock density, which is a systematic error that affects all the data points in the same way. Since the measured electron densities stay fixed, altering the preshock density moves the solid curve up or down relative to the models, which do not move appreciably as the preshock density varies by 30%.

Figure 6 indicates that B_0 is in the range 10–20 μG. We believe that the flattening out of the HH 34 compression curve

[3] Models run with "cosmic" abundances produce line ratios 2–3 times higher than observed.

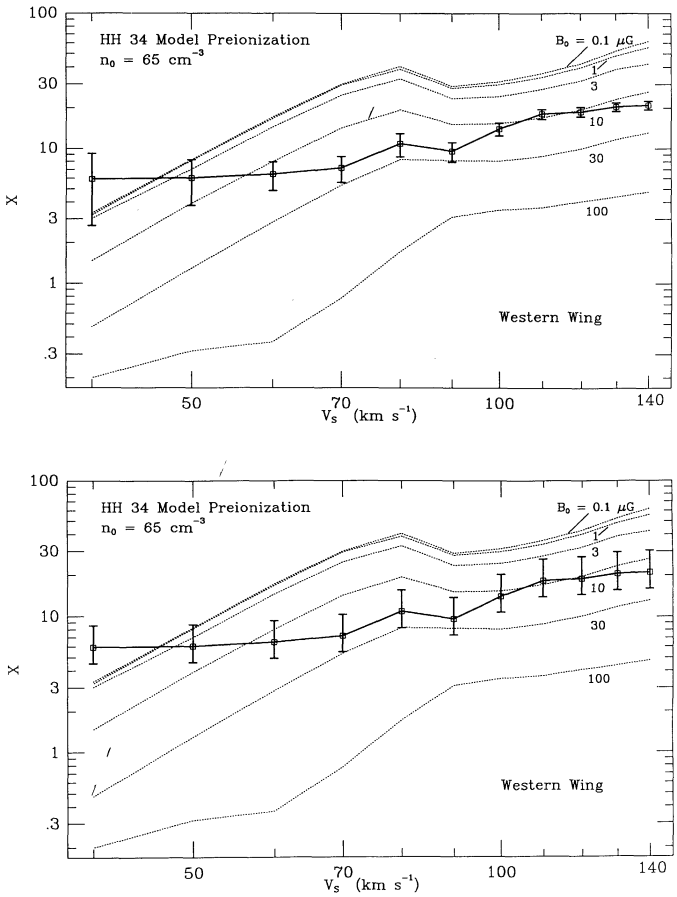

FIG. 6.—A comparison of the compressions across the western wing of the HH 34 bow shock with those predicted by planar shock models for a range in ambient magnetic field strengths. The compression, X, is defined as the ratio of the postshock electron density, as measured by the [S II] λ6716/λ6731 ratio, to the preshock density, n_0, in both the data and the models. The HH 34 data were taken from electron densities measured in the individual velocity images as a function of position and velocity along the western wing of the bow shock. The individual measurements are marked by the open boxes and are connected by the solid line. The compressions measured in the models are shown by the dotted curves. The error bars assigned to the data points in the top plot account for the statistical uncertainties in the measured electron densities. The error bars in the bottom plot account for our uncertainty in the preshock density.

toward lower shock velocities results from a gradient in the preshock density that increases toward the extreme western wing. Such a density gradient may account for the asymmetric appearance of the bow shock relative to the jet axis and the enhancement of emission in the western wing versus the eastern wing.

Table 1 reports the predicted emission-line fluxes, normalized to the flux of Hβ = 100, from our planar shock models using the Osterbrock et al. (1992) Orion abundances. The preshock ionization, n_0, and B_0 for each shock velocity are also indicated, along with the computed cooling times and distances. Our estimates of the bow shock velocity, the reddening, and preionization state of the gas could be directly tested through UV spectrophotometry. Table 1 makes definite predictions about the fluxes from very high ionization line species of C, O, N, Ne, S, and Si, all of which would be underestimated if we have underestimated the bow shock velocity, the preionization, or both.

4.1.4. *Bow Shock Model for HH 34*

We have extended HRH's bow shock code to produce two-dimensional theoretical monochromatic images and spectral grids for direct comparison with our data. As described in HRH, given a shape and shock velocity at the apex of HH 34 (§ 4.1.2), the bow shock is broken up into 200 small annuli. The flux from the desired emission line in each annulus is that produced by a plane-parallel shock of velocity $V_\perp$ weighted by the area of the annulus. The emission in each annulus is interpolated (linearly) between the fluxes given in Table 1 from the shock velocities bracketing $V_\perp$. The bow shock model is then projected onto the plane of the sky at an inclination ϕ as a function of (projected) velocity. We used a Gaussian with FWHM 40 km s^{-1} to smooth the calculated line profiles. Turbulent motions due to dynamical and thermal instabilities in the working surface, as observed in numerical simulations (Blondin, Fryxell, & Königl 1990), and unresolved geometric substructure may account for this additional line broadening. Raga & Binette (1991) have also pointed out that in the case of Hα, which appears to form primarily in the collisional zone immediately behind the shock, there would be considerable Doppler broadening due to the very high temperature of the gas in this region.

One deficiency of the bow shock model is its lack of a cooling distance in the flow, in that the model assumes that emission is confined to an unresolved thin surface of revolution around the axis of symmetry. We believe that the cooling distance *is* resolved behind the HH 34 bow shock, hence the model will not account for the spatial separation of the [S II] and Hα emission in the western wing, or more precisely, the postshock temperature structure evident in the [S II]/Hα ratio map (Fig. 4). Nor will the model predict the "knotty" structure apparent in the emission distribution, except as a result of geometric projection. Nevertheless, our model provides a meaningful reference against which to interpret the global flow properties of HH 34. Figure 7 shows the Hα velocity field predicted by the bow shock model for a systemic velocity of 0 km s^{-1}. As expected, the fluxes are highest at the apex, the line profiles along the limb-brightened edges are single peaked, and the interior profiles are double-peaked due to emission from the high-velocity foreground and low-velocity background shock surfaces.

The observed (*solid lines*) and predicted (*dotted lines*) spectral grids are directly compared in Figure 8 for each emission line that we observed. The velocity limits of each spectral bin are the same as in Figure 2. Therefore, the observed line profiles are systematically blueshifted -50 ± 10 km s^{-1} relative to the model. In general, the match between the theoretical and observed profiles is good in some regions and not so good in others. Many of our problems stem from the lack of axial symmetry for HH 34. The western wing is more oblique than the eastern wing (possibly due to a density gradient in the preshock medium), hence the conserved parallel velocity component is greater in the western wing causing the line profiles to be slightly redshifted relative to the model, whereas they are slightly blueshifted in the eastern wing.

The systematic shift of model to fit the observed line profiles corresponds to an offset from the systemic radial velocity of the HH 34 system (+25 km s^{-1}; § 4.1.1) of $V_{\rm hel} \sim -75 \pm 10$ km s^{-1}. This implies that HH 34 is moving into a medium which already has a velocity of $\sim 150 \pm 20$ km s^{-1} outward from the stellar source. This would account for the large spatial motions but the relatively low shock velocity. HR92 argue the same

TABLE 1

PREDICTED EMISSION-LINE FLUXES FROM PLANAR SHOCK MODELS WITH ORION ABUNDANCES

MODEL	S140	S130	S120	S110	S100	S090	S080	S070	S060	S050	S040
V_S (km s^{-1})	140	130	120	110	100	90	80	70	60	50	40
X (H I)	0	0	0	0	0.11	0.53	0.80	0.91	0.97	0.99	0.99
Y_0 (He I)	0	0	0	0	0.11	0.53	0.80	0.91	0.97	0.99	0.99
Y_1 (He II)	0.75	0.80	0.88	0.93	0.89	0.47	0.20	0.09	0.03	0.01	0.01
n_0 (cm^{-3})	65	65	65	65	65	65	65	65	65	65	65
B_0 (μG)	10	10	10	10	10	12	20	20	20	20	20
T_{800} (K)	1100	1650	2000	3070	3180	2150	1000	1000	1000	1750	4190
d_{c4} (AU)	82.2	39.8	27.1	26.0	26.2	22.5	11.5	7.7	10.1	17.2	39.8
d_{c3} (AU)	402	381	351	352	354	415	474	361	475	648	702
τ_{c4} (yr)	31.5	21.3	17.7	18.3	19.6	20.2	11.6	7.9	9.4	17.2	38.0
τ_{c3} (yr)	800	800	800	800	800	800	608	463	602	800	800
$F_{H\beta}$ [1]	3.90	3.17	2.46	2.02	1.79	1.97	1.73	1.04	.580	.284	.107
He II 304	4740	6640	8180	7590	5150	419	6.0	1.6	0.3	0	0
C III 977	1220	1920	2080	2120	2020	910	10.5	2.1	0.9	0.4	0.1
N III 991	170	146	112	102	93.0	43.9	0.2	0	0	0	0
O VI 1035[2]	54.9	4.3	0.4	0	0	0	0	0	0	0	0
Ne V] 1141[2]	7.2	1.7	0.5	0.1	0	0	0	0	0	0	0
S III 1198	154	153	140	135	123	82.0	2.6	0.6	0.4	0.3	0.1
Si III 1206	193	179	163	217	337	313	4.4	0.9	0.3	0.1	0
Ly α 1216	4421	4793	4886	5020	5036	5401	6205	6654	7214	8105	10175
O V] 1218	155	40.5	15.2	5.4	0.7	0	0	0	0	0	0
N V 1240[2]	301	72.7	23.2	7.6	1.0	0	0	0	0	0	0
C II 1336	250	324	415	466	465	344	18.4	11.1	10.9	13.1	20.3
Si IV 1397[2]	68.0	61.0	75.7	129	203	95.0	0.2	0	0	0	0
O IV] 1402[3]	259	128	81.2	65.7	36.7	0.6	0	0	0	0	0
N IV] 1486	96.8	54.1	32.8	26.4	17.4	0.8	0	0	0	0	0
C IV 1549	1890	2510	1950	1550	857	28.7	0.1	0	0	0	0
[Ne V] 1574	0.6	0.2	0.1	0	0	0	0	0	0	0	0
[Ne IV] 1601	11.0	6.2	4.5	3.5	1.5	0	0	0	0	0	0
He II 1640	74.7	84.2	79.1	58.6	26.6	1.1	0	0	0	0	0
O III] 1663[2]	147	129	106	99.8	94.6	44.0	0.1	0	0	0	0
N III] 1750[3]	61.3	57.5	49.7	47.5	44.0	25.0	0.2	0	0	0	0
Si III] 1891	121	122	123	148	198	194	6.8	0.9	0.3	0.2	0
C III] 1908	429	622	732	774	752	442	20.0	4.7	2.3	1.2	0.4
N II] 2141[2]	12.6	13.6	14.1	14.3	13.2	9.9	1.8	0.9	0.9	0.9	0.8
C II] 2326[3]	366	449	527	556	503	318	47.2	30.2	32.6	45.3	82.7
Si II] 2340[3]	25.0	30.4	33.2	33.0	27.3	14.2	5.3	3.5	3.7	4.9	8.7
[Ne IV] 2423[2]	55.5	32.9	25.3	20.5	9.4	0.1	0	0	0	0	0
[O II] 2470	30.8	30.4	29.7	29.1	26.3	20.5	3.9	1.4	0.8	0.6	0.4
Mg II 2799[2]	567	716	783	757	567	206	48.8	48.1	58.3	73.1	189
Mg I 2852	54.3	69.2	79.5	82.0	69.7	32.2	5.0	3.3	4.0	9.1	20.5
[O II] 3726	332	347	351	353	316	225	69.6	31.8	20.6	15.5	13.5
[O II] 3729	204	225	240	253	238	187	61.2	31.8	24.0	20.3	19.1
[Ne III] 3869	24.3	26.7	27.2	27.3	25.4	14.8	1.0	0.1	0	0	0
Ca II 3945[2]	300	316	331	331	284	138	28.5	15.3	15.2	19.9	36.3
[Ne III] 3968	7.7	8.5	8.6	8.7	8.0	4.7	0.1	0	0	0	0
[S II] 4072[2]	48.1	48.9	49.3	48.3	41.3	22.0	4.3	3.2	3.5	5.0	9.6
Ca I 4227	9.0	9.1	9.9	10.4	10.0	6.8	2.6	1.4	1.5	2.0	2.2
[O III] 4363	21.0	19.2	16.7	16.0	15.2	7.5	0	0	0	0	0
[Fe III] 4658	1.2	1.1	1.1	1.2	1.2	1.0	0.3	0.1	0	0	0
Hβ 4861	100	100	100	100	100	100	100	100	100	100	100
[O III] 4959	70.5	67.8	64.9	64.1	60.0	31.7	0.1	0	0	0	0
[O III] 5007	206	202	189	187	175	92.3	0.3	0	0	0	0
[N I] 5200[2]	38.9	56.6	71.3	76.9	68.5	33.8	8.1	6.3	9.1	17.5	44.8
[N II] 5755	5.2	5.6	5.7	5.6	4.8	3.0	0.8	0.5	0.5	0.5	0.4
He I 5876	17.2	22.6	26.2	26.7	23.5	14.6	3.6	1.8	1.0	0.5	0.4
[O I] 6300	116	158	186	190	156	67.5	14.7	15.2	23.2	38.6	76.5
[O I] 6363	38.5	52.5	62.0	63.3	52.0	22.5	4.8	5.1	7.7	12.9	25.5
[N II] 6548	86.4	93.2	94.2	91.4	74.0	39.1	14.9	10.2	10.1	10.2	8.6
Hα 6563	295	300	303	303	298	286	304	314	329	344	381

TABLE 1—*Continued*

[N II] 6583	256	276	279	271	219	116	44.3	30.2	29.7	30.3	24.2
He I 6678	5.1	6.7	7.7	7.9	7.3	5.5	1.3	0.7	0.4	0.2	0.1
[S II] 6716	167	196	225	240	223	134	39.0	32.2	44.7	73.6	152
[S II] 6731	220	243	264	273	246	142	39.3	30.4	37.4	55.7	108
[Ca II] 7307[2]	54.2	56.6	60.0	61.1	54.6	30.0	7.6	4.3	4.5	6.1	10.5
[O II] 7320	22.8	22.5	22.0	21.6	19.5	15.2	2.9	1.0	0.6	0.4	0.3
[O II] 7331	18.3	18.1	17.7	17.4	15.7	12.2	2.4	0.8	0.5	0.3	0.3
[Fe II] 8617	1.0	1.2	1.3	1.3	1.1	0.5	0.1	0.1	0.1	0.2	0.4
[C I] 8727	8.9	10.5	11.1	11.7	10.1	5.1	1.8	1.7	1.6	1.8	2.2
[S III] 9069	17.8	27.1	31.7	31.4	23.9	9.7	4.2	2.6	2.3	2.3	1.1
[S III] 9532	46.3	70.5	82.3	81.6	62.1	25.1	10.9	6.7	6.1	6.0	2.9
[C I] 9823	44.9	53.5	58.1	63.6	57.6	33.6	15.9	18.4	18.7	20.5	22.2
[C I] 9850	133	158	172	188	170	99.4	47.2	54.3	55.3	60.8	65.6
[S II]10289,339[2]	16.9	17.1	17.3	16.9	14.5	7.7	1.5	1.1	1.2	1.7	3.4
[S II]10323,373[2]	15.3	15.6	15.7	15.4	13.2	7.0	1.4	1.0	1.1	1.6	3.1
[N I]10402[2]	5.2	6.9	8.0	8.0	6.4	2.6	0.5	0.3	0.1	0.6	1.4
He I 10830	24.9	33.4	38.6	39.8	35.0	23.7	4.8	2.3	1.4	0.8	0.6
[Ne II] 12.8μ	38.1	45.2	50.7	52.3	46.6	26.8	10.2	9.8	12.6	17.3	13.4
[Ne III] 15.6μ	22.7	31.6	35.0	32.8	24.1	10.5	1.9	0.4	0.2	0.1	0
[Si II] 35.3μ	341	411	492	507	483	351	233	252	377	564	650
[O I] 63.2μ	50.8	64.6	77.4	80.7	72.6	42.1	16.5	16.5	24.6	39.6	60.0
2 photon	526	722	862	859	738	639	980	1202	1495	1958	3046

NOTE.—All fluxes are normalized to Hβ = 100. The parameters X, Y_0, and Y_1 refer to the ionization state of the preshock gas; n_0 is the preshock density; B_0 is the preshock magnetic field strength; d_{c4} and d_{c3} are the distances between the shock and the position where the postshock temperature $T = 10^4$ K and $T = 10^3$ K, respectively, while τ_{c4} and τ_{c3} are the corresponding cooling times; T_{800} refers to the postshock temperature reached when calculation of the emission-line fluxes was terminated, which was limited to a maximum cooling time of 800 yr.

[1] Flux of Hβ in units of 10^{-4} ergs s^{-1} cm^{-2} through *front* of shock.

[2] Line is a doublet.

[3] The $^4P - {}^2P$ intersystem transitions consist of five closely spaced lines (Mendoza 1983). There are seven lines of O IV] and Si IV] between 1393 and 1407 Å.

scenario for HH 34, although with a medium moving at $\sim$170 km s^{-1}, based on the radial velocity of faint emission just ahead of the bow shock. In fact, Reipurth & Heathcote (1992) have imaged a faint leading bow shock, HH 34X, $\sim$50″ downstream from HH 34. In this scenario, HH 34 is moving into the wake of the earlier ejection(s). A similar situation has been suggested for HH 47 (Hartigan, Raymond, & Meaburn 1990; Reipurth & Heathcote 1991) and for the morphologically similar HH 111 (Reipurth 1989b). Combined with our bow shock velocity of 140 ± 20 km s^{-1}, we estimate the space motion of the bow shock away from the stellar source to be $\sim 290 \pm 40$ km s^{-1}. We then predict tangential velocities in the HH 34 bow shock $\approx 260 \pm 35$ km s^{-1}, close to the 285 ± 5 km s^{-1} measured by HR92.

The ram pressure of the pre-shock gas of HH 34 is $\rho V^2 \approx 2.1 \times 10^{-8}$ ergs cm^{-3}, with $V = 140$ km s^{-1} and

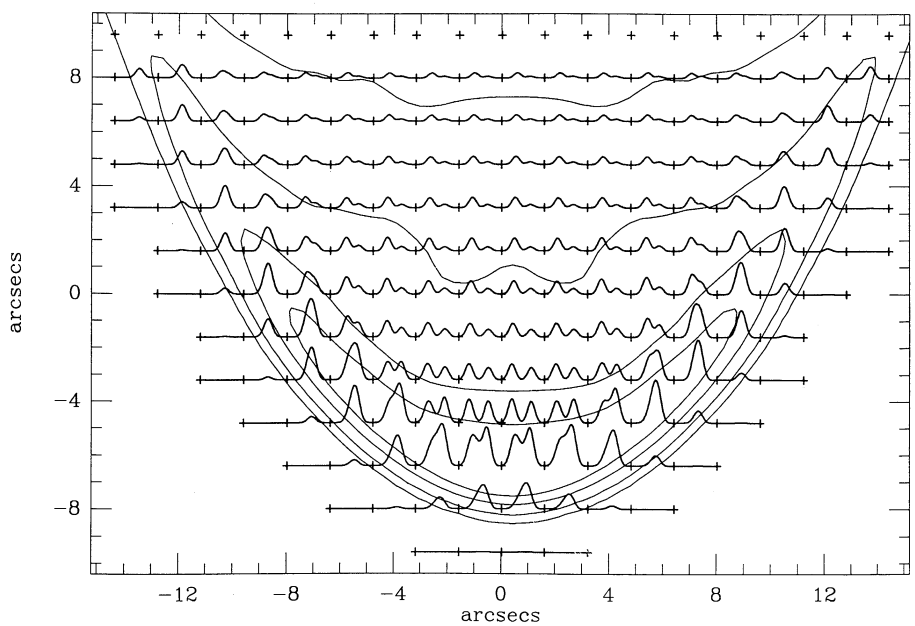

FIG. 7.—The predicted Hα velocity field produced by our model for a bow shock with shock velocity 140 km s^{-1}, viewed at an angle to the line of sight $\phi = 60°$. The line profiles are plotted with velocity limits -150 to $+120$ km s^{-1}, and have been smoothed with a Gaussian of FWHM 40 km s^{-1}.

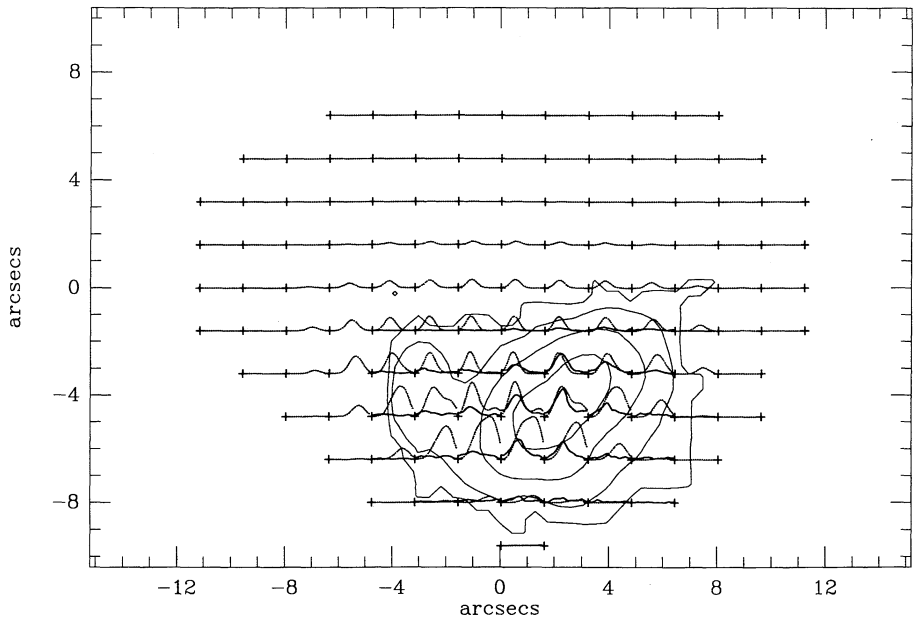

FIG. 8*a*

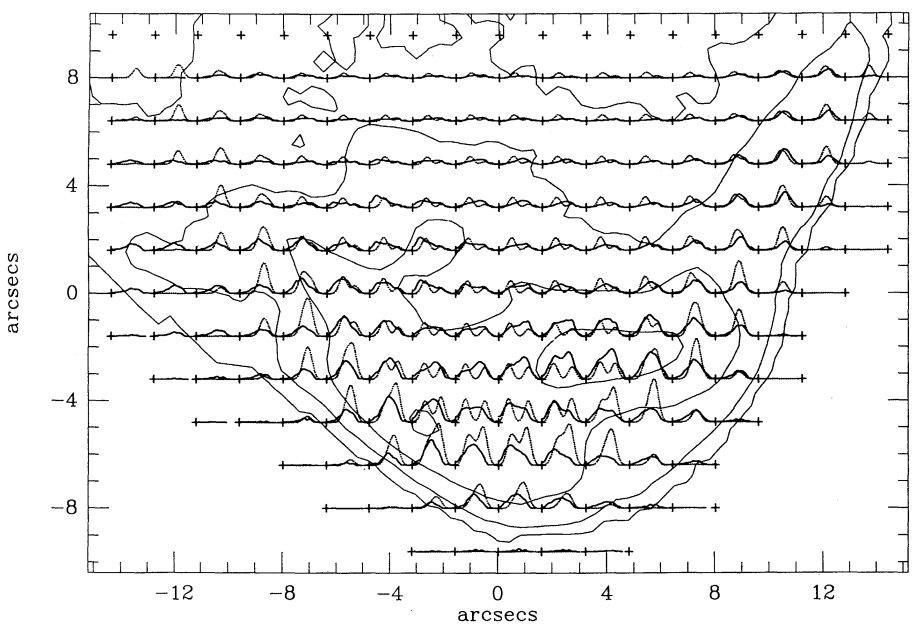

FIG. 8*b*

FIG. 8.—Observed (*solid lines*) and theoretical (*dotted lines*) spectral grids overplotted for (*a*) [O III] λ5007, (*b*) Hα, and (*c*) [S II] (λ6716 + λ6731). The model has been shifted to align with the data and the spectral profiles are plotted with the same velocity limits as in Fig. 2.

$\rho = 65 \times (1.67 \times 10^{-24})$ g cm^{-3}. From § 4.1.3, the magnetic pressure in this gas is $\sim B^2/8\pi \approx 9 \times 10^{-12}$ ergs cm^{-3}, using $B = 15$ μG. Thus, the magnetic pressure is over three orders of magnitude smaller than the ram pressure in the preshock gas of HH 34. Therefore, although the magnetic pressure plays an important role in limiting the compression of the postshock gas, the field is unimportant in the dynamics of the flow in front of HH 4. In other words, the field is carried along with the gas and is not strong enough to divert the flow ahead of HH 34 (the wake of the earlier ejection). The density and magnetic field in the bow shock of HH 34 should increase by the compression ratio X (a factor of ~ 20 at the apex, Fig. 6), while the velocity of the gas with respect to the exciting star increases to ~ 300 km s^{-1} from 150 km s^{-1}. Hence, the magnetic pressure in the bow shock is also weaker than the ram pressure of the flow by a factor of ~ 500, and the field will be carried along with the post-bow shock gas.

4.2. *Mach Disk in HH 34*

4.2.1. *Isolation of Mach Disk*

The Mach disk in the working surface HH 34 is apparently well defined in our data, in agreement with the analysis of

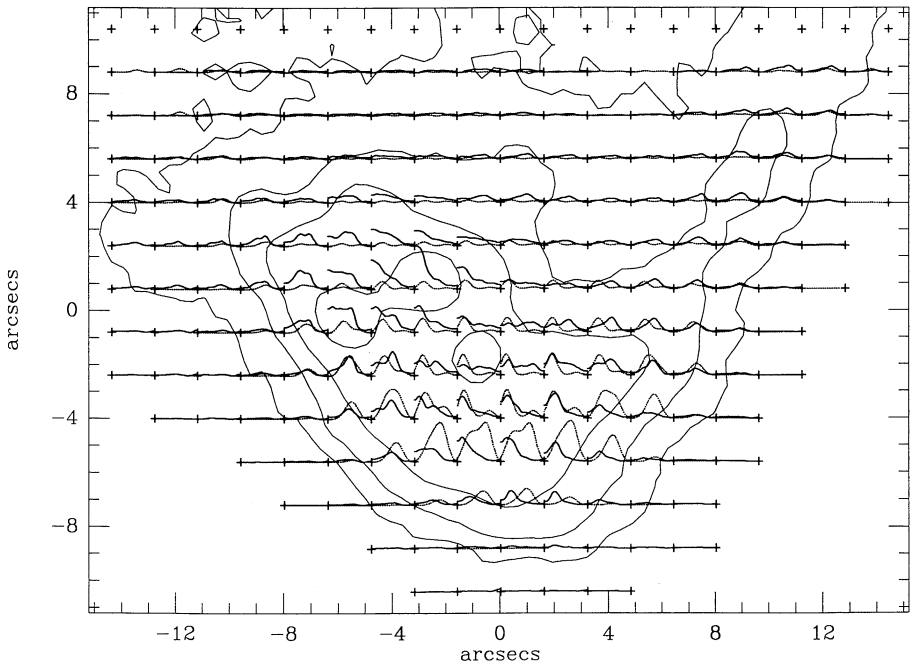

FIG. 8*c*

Hartigan (1989), who first speculated on the visibility of the Mach disk in HH 34. We confirm the conjecture by Reipurth & Heathcote (1992) that the region associated with knot F is the Mach disk, but also include the high-velocity emission from knots D and E. As evident in the spectral grids of Figure 8 and the individual monochromatic images (such as the intensity map in Fig. 3 of high-velocity [S II] emission), the Mach disk is spatially and kinematically distinct from the bow shock. The Mach disk region is characterized by low electron densities (Fig. 3) and high [S II]/Hα ratios (Fig. 4); these indicate a low shock velocity in the jet shock, implying the case of a "heavy" jet with a jet-to-ambient density ratio $n_j/n_0 = \eta > 1$.

The observed spatial separation of the bow shock emission from the Mach disk emission is several arcseconds ($\sim 5 \times 10^{16}$ cm) in HH 34. In contrast, Blondin, Königl, & Fryxell (1989) found that the recombination regions behind the Mach disk and the bow shock overlapped to produce a single dense shell of emission in their numerical simulations. The lack of agreement between the numerical models and the observations is not surprising given the complexity of the problem. The spatial separation of the two emission regions depends critically upon the details of the cooling at temperatures below 10^4 K, and the nonequilibrium cooling that is present in planar shock models has not yet been incorporated into any hydrodynamical code. In addition, the postshock magnetic field may play a role in separating the emission behind the two shocks. Our results are consistent with a dense shell of cool ($T \sim 10^3$ K), neutral atomic gas between the bow shock and the Mach disk because such a shell will not radiate strongly in either Hα, [S II], or [O III]. However, the region between the bow shock and the Mach disk must not become too dense or it will begin to form molecular hydrogen, which has not been observed in the HH 34 system (Reipurth et al. 1986; Stapelfeldt et al. 1991).

4.2.2. *Properties of Putative Mach Disk*

The spatial and kinematic emission structure of the putative Mach disk is very nonuniform, suggesting turbulent vortices at the jet head. This region accounts for ~5% of the total Hα flux from the entire working surface, but roughly one-third of the total combined [S II] flux. Note the morphology of this region in the [S II]/Hα image of Figure 4. The contact discontinuity separating post–jet shock gas from post–bow shock gas may be plausibly delineated along one of the contours that surrounds the strong [S II] emission.

The [S II]/Hα ratios in the *monochromatic* images at peak Mach disk emission range from 2.0 to 2.5 across the region, indicating an extremely low ionization state and, therefore, a low effective shock velocity. The [S II] λ6716/λ6731 ratios are near the low-density limit (>1.25; $n_e < 200$ cm^{-3}) across the region, as indicated in Figure 3. The degree of ionization in very low velocity shocks (say, 20–40 km s^{-1}) is only a few percent, so we do not expect that the electron densities indicated by the [S II] ratios reflect the true particle density in the cooling gas.

Blondin, Königl, & Fryxell (1989) note that the jet shock velocity, V_{MD} (MD = Mach disk), modified here for the moving medium, is

$$V_{MD} = V_j - (V_{BS} + V_{med}) \quad (9)$$

where V_j is the flow velocity of the jet at the working surface, V_{BS} the bow shock velocity, and V_{med} the velocity of the medium. From our previous discussion (§ 4.1), $V_{BS} = 140 \pm 20$ km s^{-1} and $V_{med} = 150 \pm 20$ km s^{-1}. In attempting to estimate V_{MD}, we note that HRH generated large [S II]/Hα ratios and low electron densities at shock velocities of 20–30 km s^{-1}. However, these characteristics can also be achieved over a large range of shock velocities (~20–60 km s^{-1}) if the magnetic field strength is a few tens of microgauss. In the following discussion, we adopt $V_{MD} \sim 40$ km s^{-1} with a probable uncertainty of ± 20 km s^{-1}. A jet shock velocity in this range implies a flow velocity for the jet of $V_j \sim 310 - 350$ km s^{-1}. Given the complicated structure of the Mach disk emission, we do not attempt a detailed model for the following reasons: (1) it is

time-dependent in simulations (e.g., Blondin et al. 1989); (2) the geometry is not obviously planar or bow-shaped in the data; and (3) there may be more than one shock present, resulting possibly in the shocks not being fully radiative as gas may pass through a second shock before cooling from the first.

Following the discussion of Hartigan (1989), we use a modified form of the relation given by Norman, Winkler, & Smarr (1983), to estimate η, the ratio of the jet density to the preshock density. Balancing the ram pressures at the jet and bow shocks,

$$\beta n_j[V_j - (V_{BS} + V_{med})]^2 = n_0 V_{BS}^2 \quad (10)$$

or

$$\beta n_j V_{MD}^2 = n_0 V_{BS}^2 , \quad (11)$$

where V_j, V_{BS}, and V_{med} are the jet flow velocity, the bow shock velocity and the velocity of the ambient medium, n_j and n_0 the jet and ambient medium densities, V_{MD} the shock velocity at the Mach disk, and β expresses the efficiency of momentum transfer from the jet to the working surface. Using values of $V_{MD} = 40$ km s^{-1}, $V_{BS} = 140$ km s^{-1}, and $n_0 = 65$ cm^{-3}, we find that $\beta n_j \approx 800$ cm^{-3}. For a heavy jet with radiative cooling, $\beta \approx 1$ (Blondin et al. 1990), implying $\eta \approx 12$. However, we emphasize that our treatment is not strictly valid over long time scales because the Mach disk is a variable structure that does not maintain a constant velocity relative to the bow shock. Despite its much higher density relative to the ambient medium, the jet head may be altered by hydrodynamical instabilities that develop over the dynamical lifetime of the flow, and may drastically modify the momentum transfer. In addition, the working surface is obviously asymmetric about the jet axis and the jet appears to be plowing into a highly nonuniform medium (as suggested in § 4.1.3).

5. CONCLUSIONS

We have performed detailed observations of the working surface HH 34 using an imaging spectrophotometer. Monochromatic images of the [S II] λ6716/λ6731 and [S II] (λ6716+λ6731)/Hα line ratios produce maps of post-shock electron densities and excitation conditions throughout the entire flow volume. We have estimated an effective bow shock velocity of 140 $\pm$ 20 km s^{-1} based on the observed bow shock shape and the spatial distribution of the [O III] λ5007 emission. A new bow shock model of HH 34 has been constructed using the geometry described in HRH and a dense grid of planar shock models with Orion abundances reported by Osterbrock et al. (1992). The model matches the observed Hα emission-line fluxes and [O III] λ5007/Hα, [S II]/Hα, and [S II] λ6716/λ6731 line ratios. We estimate that the preshock density $n_0 \approx 65$ cm^{-3}, based on the observed Hα flux at the apex of the bow shock and our estimates of the bow shock velocity and reddening toward HH 34.

Our models of HH 34 provide strong evidence that (1) the medium in front of the bow shock moves at a velocity of $\sim$150 km s^{-1} away from the source, possibly due to previous eruptions of the outflow and (2) there is separate emission from the bow shock and Mach disk in HH 34. The emission from the Mach disk occupies an irregularly shaped region at the head of the stellar jet, with a large radial velocity and a low excitation spectrum as expected from low velocity ($\sim$20–60 km s^{-1}) shocks. The jet is $\sim$10 times denser than the material in front of the bow shock of HH 34.

Given the bow shock velocity, preshock density, and postshock electron densities measured at different points along the bow shock, we estimate a magnetic field of $B_0 = 10$–20 μG in the preshock gas of HH 34, i.e., in the wake of the earlier ejection. The magnetic field inhibits the postshock compression of the gas behind the bow shock and extends the postshock cooling region to several arcseconds. However, the ram pressure of the preshock gas exceeds the magnetic energy density by at least three orders of magnitude, so that the magnetic field is *not* important in the dynamics of the flow in HH 34.

We wish to thank the staff at CTIO for their support, especially R. Schommer who operated the Fabry-Perot for each of the runs. J. A. M. also acknowledges the helpful discussions with J. Blondin, L. Hartmann, A. Raga, and B. Reipurth. We also thank the referee H.-H. Böhm for his useful suggestions for improving the manuscript, and J. Knerr and the North Carolina Supercomputing Center for the color hardcopies. J. A. M. and G. C. were supported by the NSF.

REFERENCES

Allen, C. W. 1973, Astrophysical Quantities (London: Athlone)
Atherton, P. D., Taylor, K., Pike, C. D., Harmer, C. F. W., Parker, N. M., & Hook, R. N. 1982, MNRAS, 201, 661
Bland, J., & Tully, R. B. 1989, AJ, 98, 723
Blandford, R. D., & Rees, M. J. 1974, MNRAS, 169, 395
Blondin, J. M., Fryxell, B. A., & Königl, A. 1990, ApJ, 360, 370
Blondin, J. M., Königl, A., & Fryxell, B. A. 1989, ApJL, 337, L37
Bührke, T., Mundt, R., & Ray, T. P. 1988, A&A, 200, 99 (BMR)
Cardelli, J. A., Clayton, G. C., & Mathis, J. S. 1989, ApJ, 345, 245
Cox, D. P. 1972, ApJ, 178, 143
Cox, D. P., & Raymond, J. C. 1985, ApJ, 298, 651
Hamuy, M., Walker, A. R., Suntzeff, N. B., Gigoux, P., Heathcote, S. R., & Phillips, M. M. 1992, PASP, submitted
Hartigan, P. 1989, ApJ, 339, 987
Hartigan, P., Raymond, J. C., & Hartmann, L. 1987, ApJ, 316, 323 (HRH)
Hartigan, P., Raymond, J. C., & Meaburn, J. 1990, ApJ, 362, 624
Hartmann, L. & Raymond, J. C. 1984, ApJ, 276, 560
Heathcote, S. R., & Reipurth, B. 1992, AJ, submitted (HR92)
Herbig, G. H. 1974, Lick Obs. Bull., No. 658
Lind, K. R., Payne, D. G., Meier, D. L., & Blandford, R. D. 1989, ApJ, 344, 89
McCall, M. L. 1984, MNRAS, 208, 253
Mendoza, C. 1983, in IAU Symp. 103, Planetary Nebula, ed. D. R. Flower (Dordrecht: Reidel), 143
Morse, J. A., Heathcote, S., Cecil, G., Hartigan, P., & Raymond, J. C. 1992, in preparation
Mundt, R., Brugel, E. W., & Bührke, T. 1987, ApJ, 319, 275
Norman, M. L., Winkler, K.-H. A., & Smarr, L. 1983, in Astrophysical Jets, ed. A. Ferrari & A. G. Pacholczyk (Dordrecht: Reidel), 227
Osterbrock D. E., Tran, H. D., & Veilleux, S. 1992, ApJ, 389, 305
Raga, A. C., & Binette, L. 1991, Rev. Mexicana Astron. Af., 22, 265
Raymond, J. C. 1979, ApJS, 39, 1
Raymond, J. C., Hartigan, P., & Hartmann, L. 1988, ApJ, 326, 323
Reipurth, B. 1989a, In ESO Workshop on Low-Mass Star Formation and Pre–Main-Sequence Objects, ed. B. Reipurth (Garching: ESO), 247
———. 1989b, Nature, 340, 42
Reipurth, B., Bally, J., Graham, J. A., & Zealey, W. J. 1986, A&A, 164, 51
Reipurth, B., & Heathcote, S. R. 1991, A&A, 246, 511
———. 1992, A&A, in press
Reipurth, B., Raga, A. C., & Heathcote, S. 1992, ApJ, 392, 145
Scarrot, S. M., 1988, MNRAS, 231, 1055
Shull, J. M. & McKee, C. F. 1979, ApJ, 227, 131
Solf, J., K.-H., Böhm, K.-H. 1987, AJ, 93, 1172
Solf, J., Böhm, K.-H., & Raga, A. 1988, ApJ, 334, 229
Stapelfeldt, K. R., Beichmann, C. A., Hester, J. J., Scoville, N. Z., & Gautier, T. N., III, 1991, ApJ, 371, 226